Spatial heterogeneity effects on land surface modeling of water and energy partitioning

Lingcheng Li[1], Gautam Bisht[1], L. Ruby Leung[1]

[1] Atmospheric Sciences and Global Change Division, Pacific Northwest National Laboratory, Richland, WA, USA

Correspondence to: Lingcheng Li (lingcheng.li@pnnl.gov)

8   **Abstract**

9   Understanding the influence of land surface heterogeneity on surface water and energy fluxes is

10   crucial for modeling earth system variability and change. This study investigates the effects of four

11   dominant heterogeneity sources on land surface modeling, including atmospheric forcing (ATM),

12   soil properties (SOIL), land use and land cover (LULC), and topography (TOPO). Our analysis

13   focused on their impacts on the partitioning of precipitation (P) into evapotranspiration (ET) and

14   runoff (R), partitioning of net radiation into sensible heat and latent heat, and corresponding water

15   and energy fluxes. A set of 16 experiments were performed over the continental U.S. (CONUS)

16   using the E3SM land model (ELMv1) with different combinations of heterogeneous and

17   homogeneous datasets. The Sobol' total sensitivity analysis is utilized to quantify the relative

18   importance of the four heterogeneity sources. Results show that ATM and LULC are the most

19   dominant heterogeneity sources in determining spatial variability of water and energy partitioning,

20   and their heterogeneity effects are complementary both spatially and temporally. The overall

21   impacts of SOIL and TOPO are negligible, except TOPO dominates the spatial variability of R/P

22   across the transitional climate zone between the arid western and humid eastern CONUS.

23   Comparison with ERA5-Land reanalysis reveals that accounting for more heterogeneity sources

24   improves the simulated spatial variability of water and energy fluxes. An additional set of 13

25   experiments identified the most critical components within the heterogeneity sources: precipitation,

26   temperature and longwave radiation for ATM, soil texture and soil color for SOIL, and maximum

27   fractional saturated area parameter for TOPO.

28

29

1. Introduction

Land surface heterogeneity plays a critical role in the terrestrial water, energy, and biogeochemical cycles from local to continental and global scales (Giorgi and Avissar, 1997; Chaney et al., 2018; Zhou et al., 2019; Liu et al., 2017). As the land component of global Earth System Models (ESMs) and Regional Climate Models (RCMs), land surface models (LSMs) are used to simulate the exchange of momentum, heat, water, and carbon between land and atmosphere. LSMs have been widely utilized in studies focused on climate projection, weather forecast, flood and drought forecast, and water resources management (Clark et al., 2015; Lawrence et al., 2019). At the resolutions typically applied in ESMs and RCMs, LSMs have limited ability to resolve land surface heterogeneity to skillfully represent its impacts on the surface fluxes and subsequent effects on earth system and climate simulations through land-atmosphere interactions. Singh et al. (2015) demonstrated that increasingly capturing topography and soil texture heterogeneity at finer resolutions improves the land surface modeling of soil moisture, terrestrial water storage anomaly, sensible heat, and snow water equivalent. Therefore, better representing spatial heterogeneity in land surface modeling may be crucial to reliably simulate water and energy exchange between land and atmosphere (Essery et al., 2003; Jr. et al., 2017; Fan et al., 2019; Fisher and Koven, 2020).

Several approaches have been developed to resolve land surface heterogeneity in LSMs. The most common class of method is the tile approach that subdivides each grid into several tiles to account for heterogeneous surface properties (Avissar and Pielke, 1989). The Community Land Model version 5 (CLM5) and the Energy Exascale Earth System Model (E3SM) land model (ELM) utilize a nested subgrid hierarchy in which each grid cell is composed of multiple land units, soil

52   columns, and plant functional types. Tesfa et al. (2017; 2020) developed a topography-based

53   subgrid structure based on topographic properties such as surface elevation, slope, and aspect to

54   better represent topographic heterogeneity in ELM. Swenson et al. (2019) introduced hillslope

55   hydrology in CLM5 where each grid cell is decomposed into one or more multicolumn hillslopes.

56   The second class of method to account for land surface heterogeneity is called the "continuous

57   approach" in which subgrid heterogeneity is described via analytical or empirical probability

58   density functions (PDFs) instead of dividing a grid cell into subgrid units. For example, He et al.

59   (2021) developed the Fokker-Planck Equation subgrid snow model in the Rapid Update Cycle

60   Land-Surface Model, which uses dynamic PDFs to represent the variability of snow in each grid

61   cell. The third class of method to better account for land surface heterogeneity is by developing

62   parameterizations for subgrid processes. For example, Hao et al. (2021) implemented a sub-grid

63   topographic parameterization in the ELM to represent topographic effects on insolation, including

64   the shadow effects and multi-scattering between adjacent terrains. Besides these three classes of

65   approach dealing with subgrid heterogeneity, the fourth class is to directly increase the grid

66   resolution. Previous studies have demonstrated the benefits of increasing resolution in simulating

67   precipitation, temperature, and related extreme events over multiple spatial scales (Torma et al.,

68   2015; Lindstedt et al., 2015; Cuesta-Valero et al., 2020; Koster et al., 2002; Vegas-Cañas et al.,

69   2020; Rummukainen, 2016). The proposed hyperresolution land surface modeling by Wood et al.

70   (2011) to model land surface processes at a horizontal resolution of 1 km globally and 100 m or

71   finer continentally or regionally has been gaining attention as supported by increasing availability

72   of high performance computing resources (Singh et al., 2015; Rouf et al., 2021; Ko et al., 2019;

73   Xue et al., 2021; Yuan et al., 2018; Chaney et al., 2016; Naz et al., 2018; Vergopolan et al., 2020;

74   Garnaud et al., 2016; Bierkens et al., 2014).

75

76 **There are several sources of heterogeneity in LSMs but their impact on water and energy**

77 **simulations at different spatial resolutions has not been systematically examined.** Four types

78 of heterogeneity sources are commonly categorized in land surface modeling, including

79 atmospheric forcing, soil properties, land use and land cover, and topography characteristics

80 (Singh et al., 2015; Ji et al., 2017). Singh et al. (2015) showed that including more detailed

81 heterogeneity of soil and topography at high resolutions improved the water and energy

82 simulations over the Southwestern U.S. Xue et al. (2021) demonstrated that simulations over the

83 High Mountain Asia region driven by high-resolution atmospheric forcing generally outperform

84 simulations that used coarse-resolution atmospheric forcing. Simon et al. (2020) investigated the

85 impacts of different heterogeneity sources (e.g., river routing and subsurface flow, soil type, land

86 cover, and forcing meteorology) on coupled simulations using the Weather Research and

87 Forecasting (WRF) model. They found that heterogeneous meteorology is the primary driver for

88 the simulations of energy fluxes, cloud production, and turbulent kinetic energy. Chaney et al.

89 (2016) conducted high-resolution simulations over a humid watershed and found that topography

90 and soils are the main drivers of spatial heterogeneity of soil moisture. However, these studies

91 generally focused either solely on one or few heterogeneity sources, or were conducted over small

92 domains with limited climate and hydrologic variations. Therefore, a comprehensive assessment

93 of the contribution of different heterogeneity sources to heterogeneity in energy and water fluxes

94 simulated by land surface models at continental scales is needed.

95

96 **The relative importance of heterogeneity sources on LSM simulations can be quantified by**

97 **sensitivity analysis (SA), which has been commonly used to study parametric uncertainty**

98   (Saltelli, 2002). In a quantitative sensitivity analysis, the assessed factors could include model

99   parameters as well as any other types of uncertainty induced by varying the input data (Saltelli et

100   al., 2019). The Sobol' global sensitivity analysis method is a variance-based SA approach and has

101   been widely utilized by the land surface modeling community (Rosolem et al., 2012; Nossent et

102   al., 2011; Li et al., 2013b). The most common application is assessment of model parameters

103   importance. Cuntz et al. (2016) comprehensively assessed the sensitivities of the Noah-MP land

104   surface model to selected parameters over 12 U.S. basins. This method is also utilized to quantify

105   the sensitivity of model outputs to the choice of parameterization schemes. Dai et al. (2017)

106   proposed a method based on Sobol' variance analysis to conduct sensitivity analysis while

107   simultaneously considering parameterizations and parameters. Zheng et al. (2019) utilized the

108   Sobol' method to quantify the sensitivity of evapotranspiration and runoff to different

109   parameterizations in the Noah-MP land surface model over the CONUS. Given the demonstrated

110   usefulness of the Sobol' sensitivity analysis method, it can be applied it to quantify the relative

111   importance of different heterogeneity sources on land surface water and energy simulations.

112

113   **The overarching goal of this paper is to determine the relative importance of different**

114   **heterogeneity sources on the spatial variability of simulated water and energy partitioning**

115   **over CONUS.** Four heterogeneity sources are considered in this study, including atmospheric

116   forcing (ATM), soil properties (SOIL), land use and land cover (LULC), and topography (TOPO).

117   Our analysis focuses on their impacts on the water partitioning of precipitation into

118   evapotranspiration and runoff, and the energy partitioning of net radiation into sensible heat and

119   latent heat, and their corresponding fluxes. ELMv1 is used as the model testbed. Two sets of

120   experiments are conducted with different combinations of homogeneous and heterogeneous inputs.

121   A set of 16 experiments are used to assess the impacts of the four heterogeneity sources on water

122   and energy partitioning using the Sobol' sensitivity analysis method. Subsequently, another set of

123   13 experiments are conducted to analyze the heterogeneity effects from each component of

124   atmospheric forcing, soil properties, and topography. The remaining structure of this paper is

125   organized as follows. Section 2 describes ELM, data processing, experimental design, and analysis

126   method. Results are examined in section 3, followed by discussions in section 4 and conclusions

127   in section 5.

128
129   **2. Methodology**

130   **2.1 ELM overview**

131   The E3SM is a newly developed state-of-the-science Earth system model by the U.S. Department

132   of Energy (Golaz et al., 2019; Caldwell et al., 2019; Leung et al., 2020). ELMv1 started from the

133   Community Land Model version 4.5 (CLM4.5; Oleson et al., 2013) and now includes more

134   recently developed representations of soil hydrology and biogeochemistry, riverine water, energy

135   and biogeochemistry, water management (2013a Li et al., 2013; Tesfa et al., 2014; Bisht et al.,

136   2018; Yang et al., 2019; Zhou et al., 2020). Further model developments after the ELMv1 release

137   include subgrid topographic parameterizations for solar radiation (Hao et al., 2021), a subgrid

138   topography structure (Tesfa and Leung, 2017) with subgrid downscaling of atmospheric forcing

139   (Tesfa et al., 2020), and plant hydraulics (Fang et al., 2021). However, these new developments

140   are not included in this study.

141

142   **2.2 ELM inputs**

143   **2.2.1 Heterogeneity sources**

144   ATM forcing for ELM consists of seven surface meteorological variables, including precipitation

145   (PRCP), air temperature (TEMP), specific humidity (HUMD), shortwave radiation (SRAD),

146   longwave radiation (LRAD), wind speed (WIND), and air pressure (PRES). Atmospheric forcing

147   from the North American Land Data Assimilation System phase 2 (NLDAS) is used in this study

148   (Xia et al., 2012b, a). SOIL consists of soil texture (STEX), organic matter content (SORG), and

149   soil color (SCOL). STEX and SORG determine soil thermal and hydrologic properties, while

150   SCOL regulates the soil albedo and hence surface energy related processes. LULC consists of the

151   glacier, lake, and urban fractions, the fractional cover of each plant functional type (PFT), and

152   monthly leaf area index (LAI) and stem area index (SAI) for each PFT. The high-resolution

153   datasets of land use land cover, leaf area index, and stem area index at 0.05°×0.05° developed by

154   Ke et al. (2012) are used for LULC in this study. TOPO consists of the standard deviation of

155   elevation (SD_ELV), maximum fractional saturated area (Fmax), and topography slope. TOPO is

156   used in snow cover parameterization, surface runoff generation and infiltration, etc. SOIL and

157   TOPO datasets are obtained from the NCAR dataset pool for CLM5 (Lawrence et al., 2019;

158   Lawrence and Chase, 2007; Bonan et al., 2002; Batjes, 2009; Hugelius et al., 2013; Lawrence and

159   Slater, 2008). Table 1 summarizes these heterogeneity components and resolutions of the source

160   data. All datasets were prepared over the entire CONUS.

161   Table 1 Summary of heterogeneity sources in ELM model inputs

Heterogeneity source	Components	Source data resolution
ATM	Precipitation, air temperature, specific humidity, shortwave radiation, longwave radiation, wind speed, air pressure	0.125°, hourly
SOIL	Soil texture, soil organic matter	0.083°, static
	Soil color	0.5°, static
TOPO	Slope, Standard deviation of elevation, maximum fractional saturated area	0.125°, static
LULC	Fractions of PFTs, wetland, lake, urban characteristics, and glacier	0.05°, static
	Leaf area index (LAI) for each PFT	0.05°, monthly

162

163 **2.2.2 Heterogeneous and homogeneous inputs**

164 We prepared heterogeneous and homogeneous inputs at 0.125°×0.125°. The difference between

165 the two datasets is whether the input values within each 1°×1° region of ELM are spatially

166 heterogeneous or homogeneous. The four types of datasets listed in Table 1 were first resampled

167 to 0.125°×0.125° resolution from their original resolutions, which are used as the heterogeneous

168 inputs (Figures 1a and 1b). Then, for each dataset, we replaced the heterogeneous values of the 64

169 0.125°×0.125° grids within each 1°×1° region by the mean of the 64 grids (see Figure 1b vs. 1d).

170 The temporally varying datasets (e.g., hourly ATM and monthly climatology LAI) were processed

171 at each time interval. As an example, Figure 1 compares the annual climatology of the

172 heterogeneous and homogeneous precipitation.
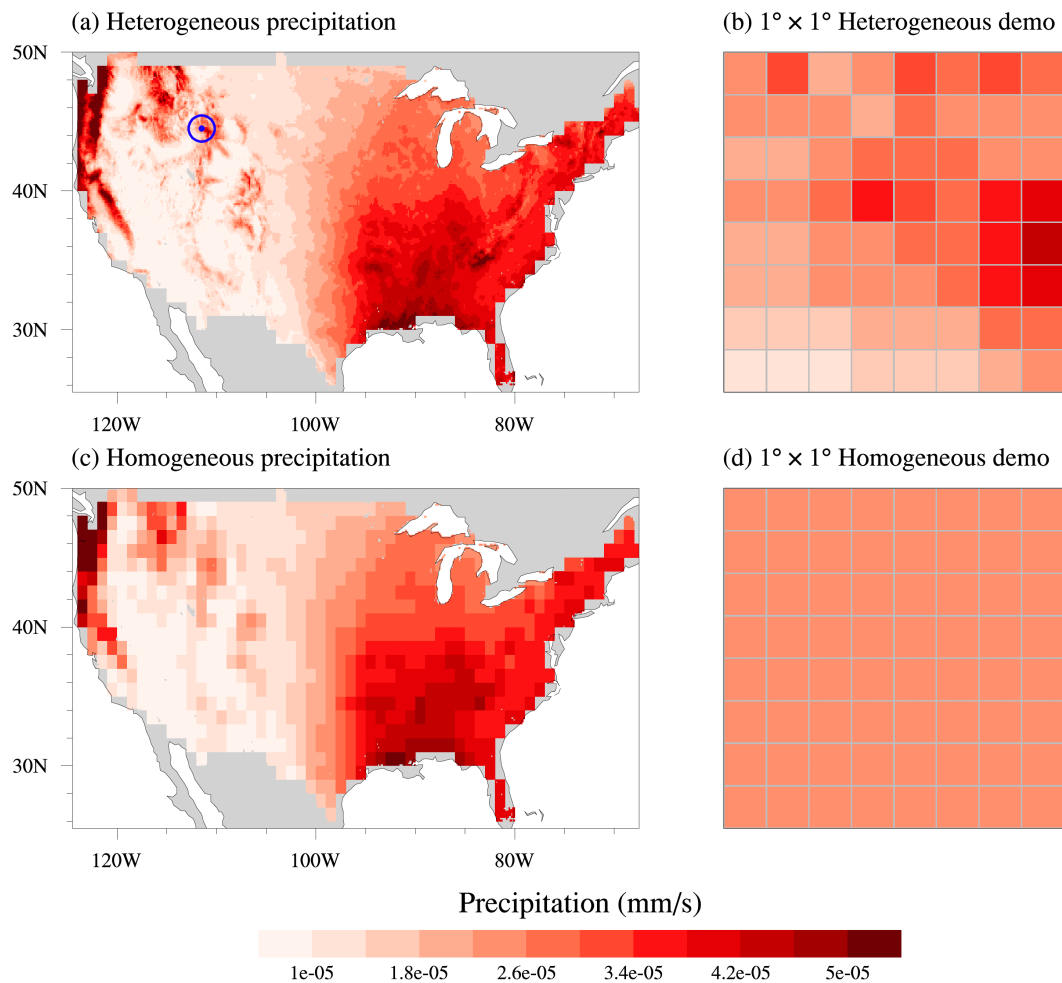
Figure 1. Annual climatology of (a) heterogeneous and (c) homogeneous precipitation over CONUS. The corresponding (b) heterogeneous and (d) homogeneous precipitation over a 1°×1° region (latitude: 37° N ~ 38° N, longitude: 111° W ~ 110° W, the blue marker in (a)) is also shown.

2.3 Experimental design and analysis

We conducted two sets of ELM experiments over CONUS. The first set contains 16 experiments with different combinations of heterogeneous and homogeneous inputs from the four heterogeneity

181   sources (Table 2). These experiments were used to quantify the influence of different heterogeneity

182   sources on the ELM simulations. The second set of 13 experiments were further conducted to

183   analyze the impact of heterogeneity from individual components of three heterogeneity sources

184   (Table 3). As LULC has no explicit individual component, we only analyzed the components of

185   ATM with seven experiments, SOIL with three experiments, and TOPO with three experiments.

186   Each experiment only contains one heterogeneous input while other components are homogeneous.

187   Both the first and second set of experiments were configured at 0.125°×0.125° spatial resolution.

188   The 40-year NLDAS-2 forcing from 1980–2019 was cycled twice to drive the ELM run for 80

189   years. The first 50-year run was used as model spin-up, and the last 30-year simulation

190   (corresponding to atmospheric forcing from 1990–2019) was used for further analysis.

191

192   Table 2. The first set of 16 experiments with inputs from ATM, SOIL, LULC, and TOPO.
193   (0 and 1 denote homogeneous and heterogeneous input from the four heterogeneity sources,
194   respectively)

No.	Abbr.	ATM	SOIL	LULC	TOPO
EXP1	A0S0L0T0	0	0	0	0
EXP2	A0S0L0T1	0	0	0	1
EXP3	A0S0L1T0	0	0	1	0
EXP4	A0S0L1T1	0	0	1	1
EXP5	A0S1L0T0	0	1	0	0
EXP6	A0S1L0T1	0	1	0	1
EXP7	A0S1L1T0	0	1	1	0
EXP8	A0S1L1T1	0	1	1	1
EXP9	A1S0L0T0	1	0	0	0
EXP10	A1S0L0T1	1	0	0	1
EXP11	A1S0L1T0	1	0	1	0
EXP12	A1S0L1T1	1	0	1	1
EXP13	A1S1L0T0	1	1	0	0
EXP14	A1S1L0T1	1	1	0	1
EXP15	A1S1L1T0	1	1	1	0
EXP16	A1S1L1T1	1	1	1	1

195

196   Table 3. The second set of 13 experiments with inputs from each component of the heterogeneity

197   sources.

No.	Sole heterogeneity input
ATM	
ATM1	Precipitation
ATM2	Air temperature
ATM3	Specific humidity
ATM4	Shortwave radiation
ATM5	Longwave radiation
ATM6	Wind speed
ATM7	Air pressure
SOIL	
SOIL1	Soil texture of sand, silt, and clay
SOIL2	Soil organic matter
SOIL3	Soil color
TOPO	
TOPO1	Fmax
TOPO2	Standard deviation of elevation
TOPO3	Slope

198

199   Our analysis focused on water partitioning, energy partitioning, and related flux variables. The

200   water partitioning is quantified as the ratio between evapotranspiration (ET) and precipitation (P),

201   i.e., ET/P, and the ratio between runoff (R) and precipitation (P), i.e., R/P. The energy partitioning

202   is quantified using the evaporative fraction (EF), which equals the ratio between latent heat (LH)

203   and the sum of latent heat and sensible heat (SH), i.e., $EF = LH/(LH + SH)$. Based on outputs

204   from each experiment, the 30-year monthly, seasonal, and annual climatological means were first

205   calculated at 0.125°×0.125° resolution for the five variables of interest (i.e., P, ET, R, LH, and SH).

206   Second, the water and energy partitioning variables (i.e., ET/P, R/P, EF) were computed at

207   0.125°×0.125° resolution. Third, the standard deviations (SD) of these variables were calculated

208   for each 1° × 1° region from the encompassed 64 0.125°×0.125° grids. These 1° x 1° resolution

209   SDs of the first and second set of experiments were used in following analysis.

210   For the first set of 16 experiments, we utilized the Sobol' sensitivity analysis to quantify the relative

211   importance of the four heterogeneity sources on water and energy simulations. Detail of the Sobol'

212   sensitivity analysis is described in section 2.4.

213   The Sobol' method was not used for the second set of 13 experiments because a comprehensive

214   Sobol' analysis needs 2^{13} experiments, which is computationally infeasible. Instead, the calculated

215   SD of each experiment is used to quantify the impact of heterogeneity of each component, as each

216   experiment only contains one heterogeneous input. Therefore, we compared the SDs between each

217   experiment to determine the relative importance of each component with heterogeneous input

218   (without considering interactions between different components).

219

220   2.4 The Sobol' total sensitivity index

221   The Sobol' sensitivity analysis (Sobol', 1993) was applied to quantify the sensitivity of spatial

222   variation (i.e., SD) of water and energy partitioning to the four heterogeneity sources based on the

223   first set of 16 experiments. The Sobol' total sensitivity index, SI_{X_i}, is given as,

224   $$SI_{X_i} = \frac{E_{X_{\sim i}}(V_{X_i}(Y|X_{\sim i}))}{V(Y)} \tag{1}$$

225   where X_i ($i = 1,2,3,4$) is the i-th heterogeneity source (e.g., ATM, SOIL, LULC, and TOPO); $X_{\sim i}$

226   denotes the other heterogeneity factors except X_i; Y represents the corresponding SDs for a given

227   simulated variable of all 16 experiments. $V(Y)$ is the total variance of all the 16 SDs. The SDs of

228   the 16 experiments are then reformed into 8 subgroups based on experiments with different

229   combinations of $X_{\sim i}$; $V_{X_i}(Y|X_{\sim i})$ denotes the variance of SDs of each subgroup of experiments

230   with heterogeneous and homogeneous inputs of X_i; $E_{X_{\sim i}}$ is the arithmetic average across different

231   combinations of heterogeneity sources other than X_i.

232   Table 4 demonstrates the calculation of the Sobol' index to quantify the sensitivity of EF spatial

233   variability to LULC in a 1° × 1° region at 39.5N and 107.5W. The 16 experiments are grouped

234   into eight subgroups containing two experiments, where the difference between the two

235   experiments in a given subgroup is homogeneous vs. heterogeneous LULC. The SDs of the 16-

236   experiments are listed in C1. The variance of each subgroup is computed in C2, which represents

237   the influence of LULC heterogeneity. The average impact of LULC heterogeneity from the eight

238   subgroups in C3 is computed as the mean of values in C2. The total variance of these 16 SDs in

239   C1 is computed in C4. Finally, the ratio between C3 and C4 is calculated as Sobol' total sensitivity

240   index in C5, which quantifies EF spatial variability sensitivity to LULC heterogeneity. The Sobol'

241   total sensitivity index for ATM, TOPO, and SOIL index can be computed similarly.

242   Table 4 Demonstration of Sobol' index calculation of the sensitivity of EF spatial
243   variability to LULC

Experiments	Y	$V_{LULC}(Y\|X_{\sim LULC})$	$E_{\sim LULC}(V_{LULC}(Y\|X_{\sim LULC}))$	$V(Y)$	SI_{LULC}
C0	C1	C2	C3	C4	C5
A0S0L0T0	0.00	6.88			
A0S0L1T0	5.24				
A0S0L0T1	0.57	6.28			
A0S0L1T1	5.58				
A0S1L0T0	0.32	6.75			
A0S1L1T0	5.51				
A0S1L0T1	0.69	6.64			
A0S1L1T1	5.84		3.32	26.99	0.12
A1S0L0T0	12.88	0.01			
A1S0L1T0	12.67				
A1S0L0T1	12.80	0.00			
A1S0L1T1	12.76				
A1S1L0T0	12.71	0.01			
A1S1L1T0	12.51				
A1S1L0T1	12.63	0.00			
A1S1L1T1	12.59				

244

245   **2.5 ERA5-Land reanalysis dataset**

246   We further compared the first set of experiments with ERA5-land reanalysis (the land component

247   of the fifth generation of European Centre of Medium-range Weather Forecast reanalysis) (Muñoz-

248   Sabater et al., 2021) to demonstrate the added value in ELM simulations with consideration of

249   heterogeneity sources. ERA5-Land provides a consistent view of terrestrial water and energy

250   cycles at high spatial and temporal resolutions. The monthly ERA5-Land data at 0.1°×0.1°

251   resolution was used in this study. First, the monthly data was resampled to 0.125°×0.125°

252   resolution. Second, the annual and seasonal climatological means for related variables (e.g., ET,

253   R, SH) were computed. Third, SD for each variable was calculated within each 1°×1° region for

254   further comparisons with the ELM simulations.

255

256 **3. Results**

257 **3.1. CONUS overall heterogeneity sensitivities**

258 The inclusion of more heterogeneity sources leads to larger spatial variability in the simulated

259 ET/P, R/P, and EF (Figure 2). For example, comparing experiment A0S0L0T0 with A1S0L0T0

260 that includes the ATM heterogeneity, the CONUS averaged SD for ET/P increases from 0 to 4.7%

261 (Figure 2a). By further comparing experiments in the first and third rows with the second and

262 fourth rows, ATM always increases the spatial variability of water and energy partitioning.

263 Similarly, LULC heterogeneity also shows large impacts on the spatial variability for the

264 partitioning variables as indicated by comparing experiments in the first and third columns with

265 the second and fourth columns. However, heterogeneity in SOIL and TOPO show negligible

266 impact. The effects of the heterogeneity sources on the spatial variability of water and energy

267 partitioning are mainly located in western and central CONUS (Figure S1), which is consistent

268 with the spatial variability of the heterogeneity inputs, for variables such as precipitation, air

269 temperature, and longwave radiation (Figure S2).
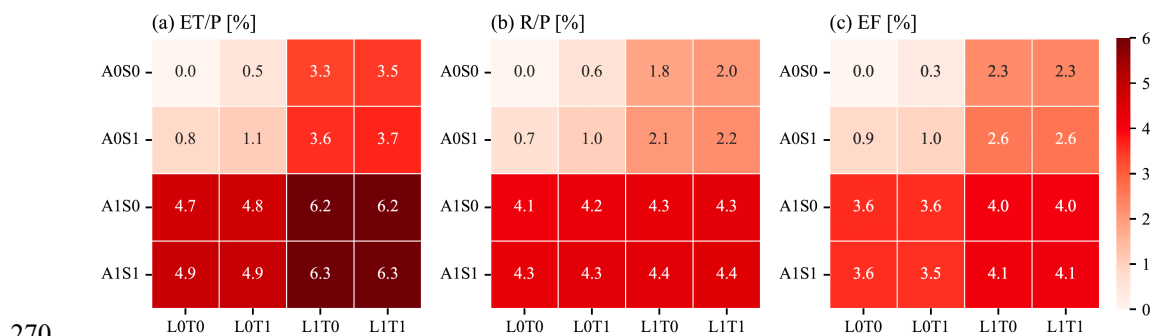
271 Figure 2. CONUS averaged SD of the annual climatology of (a) ET/P, (b) R/P, and (c) EF.

272 Combining the X-axis label for LULC and TOPO and the Y-axis label for ATM and SOIL

273 indicates the names of the experiments listed in Table 2, highlighting the use of heterogeneous

274 (1) and homogeneous (0) inputs for each heterogeneity source.

275

276   ATM, with the largest Sobol' sensitivity index, is the most important heterogeneity source to

277   determine the spatial variability of water and energy partitioning (Figure 3). LULC is the second

278   most important heterogeneity source. However, the heterogeneity of SOIL and TOPO marginally

279   contribute to the spatial variability of water and energy partitioning. Even though ATM dominates

280   the spatial heterogeneity of total ET, LULC is the main contributor to the spatial variability of the

281   ET components of transpiration, canopy evaporation, and ground evaporation. TOPO shows larger

282   impacts on the spatial variabilities of the runoff components than the total runoff.
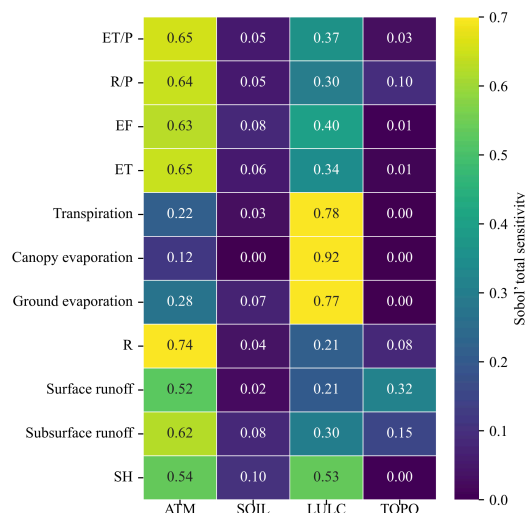
283

284   Figure 3. CONUS averaged Sobol' sensitivity index for the sensitivity of spatial variability of

285   different variables (rows) to the four heterogeneity sources (columns).

286
287   **3.2 Spatial patterns of heterogeneity sensitivities**

288   The sensitivity of the four heterogeneity sources shows different spatial patterns over CONUS

289   (Figure 4). The water partitioning components, ET/P and R/P, exhibit similar spatial patterns of

290   Sobol' sensitivity index for any given heterogeneity source (Figures 4a-d, 4f-i). ATM shows high

291   Sobol' sensitivity index over most CONUS regions for water and energy partitioning. It dominates

292   the spatial variability of ET/P and R/P over eastern and western CONUS but not central CONUS

293   (Figures 4e and 4j). For the spatial variability of EF, ATM mostly shows dominant effects over

294   central and western CONUS (Figures 4o). LULC is the second most dominant heterogeneity

295   source and dominates most regions over eastern CONUS (Figure 4o), although LULC also

296   dominates smaller regions for the spatial variability of ET/P and R/P over central and southeastern

297   CONUS (Figures 4e and 4j). Although TOPO overall has low Sobol' index, it dominates the spatial

298   variability of R/P over central CONUS (Figure 4j). SOIL has negligible impacts over most regions

299   of CONUS for the spatial variability of both water and energy partitioning.
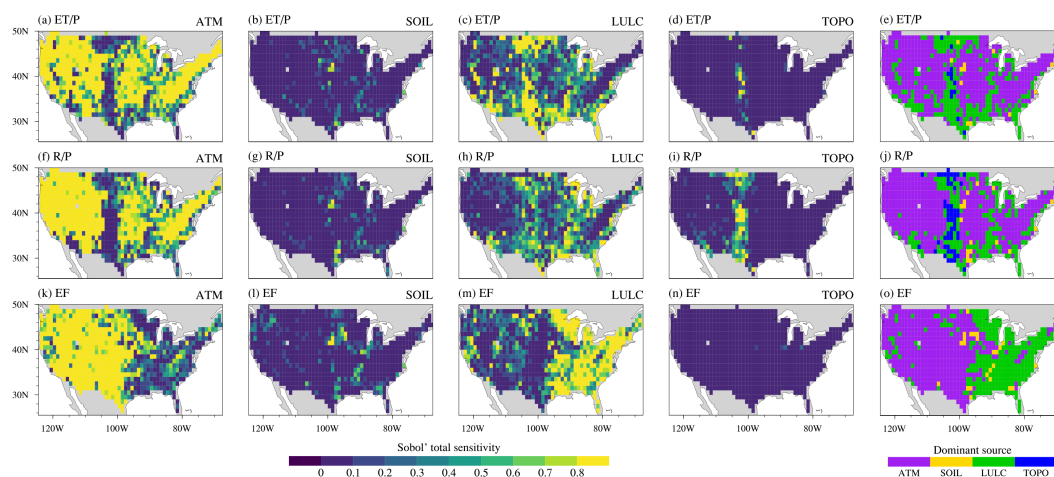

300

301   Figure 4. Spatial patterns of Sobol' total sensitivity index to the four heterogeneity sources

302   (column 1-4) and the corresponding dominant sources (column 5) for the spatial variability of

303   water (ET/P and R/P) and energy (EF) partitioning.

304

305   To further explain the spatial patterns of the Sobol' index for the two most dominant heterogeneity

306   sources of ATM and LULC, we further analyzed EXP9 (A1S0L0T0) and EXP3 (A0S0L1T0) listed

307   in Table 2. EXP9 and EXP3 only include heterogeneous inputs from ATM and LULC, respectively.

308   Let us consider ET/P as the quantity of interest for the following discussion. First, the SD of ET/P

309   is computed from the annual climatology (see section 2.3). Next, the SD ratio of ET/P, denoted as

310    $SDR_{ET/P}$, is computed as the ratio between the SD of ET/P in EXP9 and EXP3. $SDR_{ET/P}$

311   represents the relative spatial variability induced by ATM compared to LULC (Figure S3a). The

312   spatial pattern of the ATM Sobol' index for the ET/P spatial variability shows a positive

313   relationship with the spatial pattern of $SDR_{ET/P}$ (purple circles in Figure 5a, corresponding to

314   Figure 4a vs. Figure S3a). Therefore, a higher value of $SDR_{ET/P}$ indicates that relative to LULC,

315   ATM induces larger ET/P spatial variability, and hence has a higher ATM Sobol' index. Similarly,

316   a lower value of $SDR_{ET/P}$ indicates LULC induces larger ET/P spatial variability than ATM, and

317   hence has a higher LULC Sobol' index (green circles in Figure 5a). Similarly, $SDR_{R/P}$ and SDR_{EF}

318   were calculated for R/P and EF, and they also show a positive (negative) relationship with the

319   corresponding ATM (LULC) Sobol' index (Figures 5b and 5c, and Figures S3b and S3c). We can

320   also see that the ATM Sobol' index has opposite spatial patterns compared to that of the LULC

321   Sobol' index. Therefore, ATM and LULC show complementary contributions to the spatial

322   variability of water and energy partitioning across CONUS.
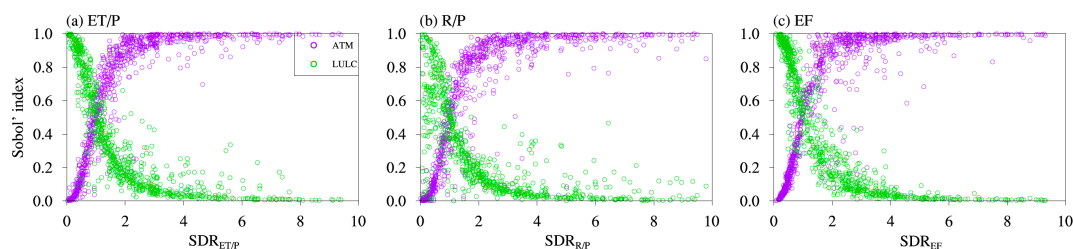
323

324   Figure 5. CONUS spatial relationship between the ATM and LULC Sobol' sensitivity index and

325   the SD ratio for (a) ET/P, (b) R/P, (c) EF. The y-axis values correspond to the spatial patterns of

326   the Sobol' index for ATM (purple) and LULC (green) in Figure 4 (i.e., each circle corresponds to

327   each 1°×1° region in Figure 4). The x-axis corresponds to the spatial pattern of the SD ratio in

328   Figure S3.

329

3.3 Seasonal variation of heterogeneity sensitivities

331   The impacts of ATM and LULC on the spatial variability of water and energy fluxes show more

332   seasonal variations than the impacts of SOIL and TOPO (Figure 6, SOIL and TOPO are not shown

333   here). This is because ATM and LULC consist of time-varying inputs to the ELM simulations, but

334   SOIL and TOPO are time-invariant inputs. Even though the spatial distribution of LULC is

335   temporally static, the monthly variations in LAI and SAI of different land cover types could affect

336   the seasonal variation of sensitivity. The heterogeneity impacts of ATM and LULC on the spatial

337   variability of water and energy fluxes show complementary seasonal variations. The effect of

338   ATM on the ET spatial variability is larger in July–September than in other months (Figure 6a),

339   while LULC shows smaller Sobol' index in July–September. The sensitivity of transpiration and

340   canopy evaporation shows the same seasonal variations (Figures S4a~c). The spatial variability of

341   R is more sensitive to ATM in the cold season (December–April, Figure 6b), especially for its

342   component of surface runoff (Figure S4d). The sensitivity of SH spatial variability to ATM is

343   larger in the non-growing season (i.e., November–March) than in the growing season (i.e., April–

344   October), with the LULC Sobol' index showing opposite seasonal variations.

345

346   To further explain the seasonal variations of the Sobol' index for ATM and LULC, the SD of ET

347   for each month was calculated as an example from monthly mean climatology and the SD ratio for

348   each month was computed as the ratio between the SD of ET in EXP9 and EXP3. For each 1°×1°

349   region, the 12 monthly SD ratios were normalized to [0, 1] using minimum and maximum values.

350   Finally, the CONUS average of the normalized SD ratios was computed for each month, denoted

351   as $NSDR_{ET}$. A higher value of $NSDR_{ET}$ denotes ATM induces more ET spatial variability than

352   LULC. Therefore, $NSDR_{ET}$ shows similar seasonal variations with the ATM Sobol' index for ET

353   spatial variability (black curve vs. purple curve in Figure 6a), but opposite seasonal variations with

354   the LULC Sobol' index (black curve vs. green curve in Figure 6a). Similarly, $NSDR_R$ and $NSDR_{SH}$

355   were calculated for R and SH, and they also show a similar (opposite) seasonal variation with the

356   corresponding seasonal ATM (LULC) Sobol' index (Figures 6b and 6c).

357
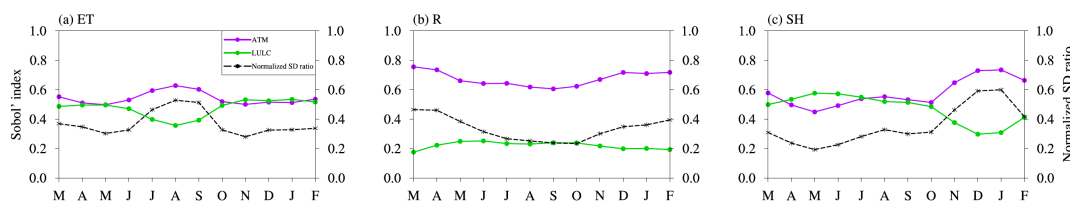
358   Figure 6. Monthly variations of CONUS averaged ATM and LULC Sobol' index and normalized

359   SD ratio for (a) ET, (b) R, and (c) SH.

360

361   The spatial patterns of dominant regions by the four heterogeneity sources vary over different

362   seasons. Compared with spring and winter, ATM dominates the ET spatial variability in more

363   regions than in summer and fall when ATM is more dominant over eastern CONUS (Table 5 and

364   Figures S5a~d). LULC shows opposite seasonal spatial patterns with more dominant regions in

365   eastern CONUS over spring and winter. As for the R spatial variability, TOPO shows large spatial

366   variation of its dominant regions over different seasons (Figures S5f~i). Besides its dominant

367   contribution in central CONUS over all seasons, TOPO also dominates the R spatial variability in

368   parts of eastern US in the summer and autumn (Figures S5g~h). For the EF spatial variability,

369   ATM has more contributions in the fall and winter but smaller contributions in spring and summer

21

Geoscientific
Model Development
Discussions

370   than LULC (Table 5). LULC shows more dominant regions over eastern CONUS, especially in

371   spring and summer (Figures S5k~i).

372   Table 5 Grid percentage of the dominant heterogeneity source in determining the spatial
373   variability of ET, R, and SH for four seasons and annual mean (ANN)

| Seasons	ATM	SOIL	LULC	TOPO
ET				
Spring (MAM)	51	4	46	0
Summer (JJA)	63	3	34	0
Fall (SON)	57	2	42	0
Winter (DJF)	49	0	51	0
ANN	66	2	31	0
R				
Spring (MAM)	81	2	13	5
Summer (JJA)	67	4	17	11
Fall (SON)	66	6	18	11
Winter (DJF)	75	2	12	10
ANN	77	1	15	7
SH				
Spring (MAM)	44	5	51	0
Summer (JJA)	45	2	53	0
Fall (SON)	52	5	44	0
Winter (DJF)	69	2	29	0
ANN	49	4	47	0

374

3.4 Effects of ATM heterogeneity components

376   Based on the second set of 13 experiments, we analyzed the heterogeneity effects by each

377   component of ATM, SOIL, and TOPO (Figure 7), respectively. Precipitation is the largest ATM

378   heterogeneity source in determining the spatial variability of water fluxes (Figures S6a~b),

379   especially over western and central CONUS for ET (Figure 7a) and almost the entire CONUS for

380   R (Figure 7b). Air temperature dominates the spatial variability of ET in eastern CONUS (Figure

381   7a). The spatial variability of SH is mainly dominated by the incoming longwave radiation in

382   western CONUS and by the air temperature in eastern CONUS (Figure 7c). Longwave radiation

383   provides more energy input and contributes more to the SH spatial variability than shortwave

384   radiation (Figure S6c). Among the SOIL components, soil texture, which can influence soil

385 moisture and runoff generation, shows the largest effects on the ET and R spatial variability over

386 most CONUS regions (Figures 7d and 7e). Soil color, affecting the surface albedo and energy

387 balance, shows the largest impacts on the SH spatial variability over central CONUS (Figures 7f

388 and 8f). Fmax is the most essential TOPO component, offering the largest effects on the spatial

389 variability of ET, R, and SH over most CONUS regions (Figures 7g~i and Figures S6g~i). Fmax

390 regulates surface runoff generation and infiltration, and therefore influences the soil moisture, ET,

391 and SH. SD_ELV and slope can affect surface water and snow cover fraction, and consequently,

392 they show the largest impacts over northwestern CONUS regions with mountains and snowpack.

393 The spatial variability induced by all components (of ATM, SOIL, or TOPO) is larger than that

394 induced by each individual component. However, it is smaller than the sum of the spatial

395 variability induced by each component (Figure S6). For example, the CONUS averaged SD for

396 ET caused by all SOIL components is 1.9 (10^{-7} mm/s), which is smaller than 2.5 (10^{-7} mm/s), the

397 sum of the SD of ET induced by STEX, SORG, and SCOL (Figure S6d). Therefore, the additional

398 SD induced by an additional heterogeneity component decreases, suggesting that the effect of

399 heterogeneity on the spatial variability of water and energy fluxes saturates, possibly due to

400 interactions among the processes influenced by the heterogeneity sources.
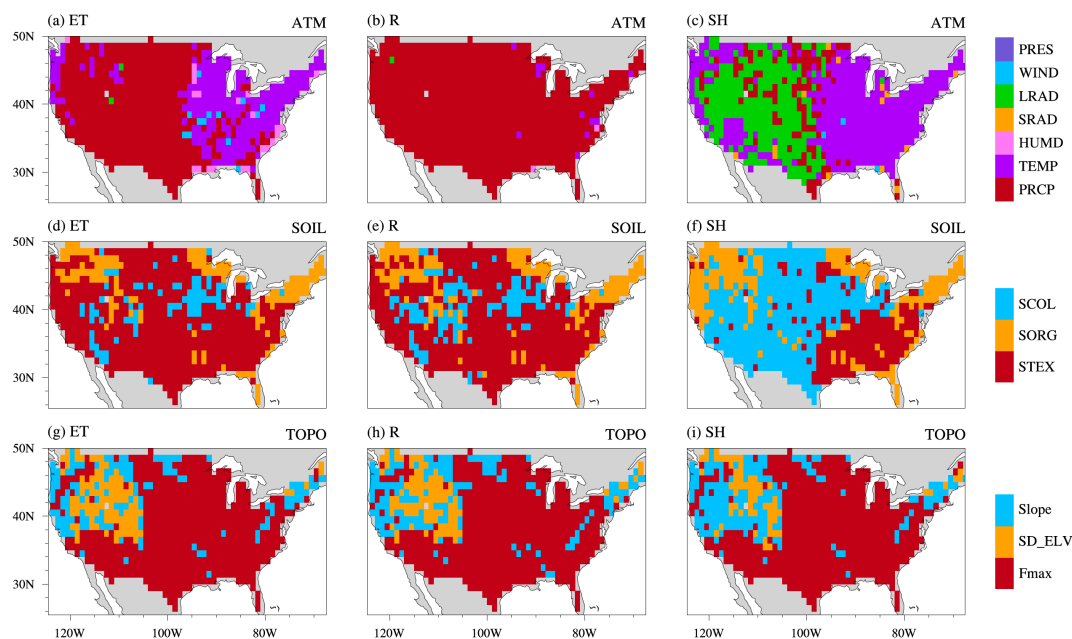
Figure 7. The largest induced spatial variability for the annual climatological mean of ET (left column), R (middle column), and SH (right column) induced by each component of ATM (top panel), SOIL (middle panel), and TOPO (bottom panel)

3.5 Comparison with ERA5-Land reanalysis

Higher consistency of the spatial variability between the simulations and ERA5-Land reanalysis (i.e., smaller SD difference) is obtained when more sources of heterogeneity are accounted for in the simulations for ET, R, and SH (Figure 8). ATM and LULC dominate the improvements of the spatial variability of model simulations. Generally, ATM heterogeneity leads to more or similar improvements than LULC heterogeneity for ET, R, and SH over all seasons. For example, in Figure 8a, ATM induced larger improvements, as shown by comparing experiments in the first and third rows with the second and fourth rows, than the LULC induced improvements, comparing experiments in the first and third columns with the second and fourth columns. The SD difference is usually larger over MAM and JJA than SON and DJF, probably due to the heterogeneity

416   difference between the NLDAS and ERA5 atmosphere forcing as ATM is the major heterogeneity

417   contributor. Improvements of the spatial variability of model simulations are primarily distributed

418   over western and eastern CONUS for ET and R, and western CONUS for SH (e.g., Figures S7 1st

419   column vs. 4th column). For ET and R, ATM mainly improves their spatial variability over western

420   and eastern CONUS (Figures S7a vs. S7c, and S7e vs. S7g), and LULC mostly shows

421   improvements over eastern CONUS (Figures S7a vs. S7b, and S7e vs. S7f). Both ATM and LULC

422   show improvements in the SH spatial variability over western and eastern CONUS (Figure S7i vs.

423   S7j, and S7i vs. S7k).
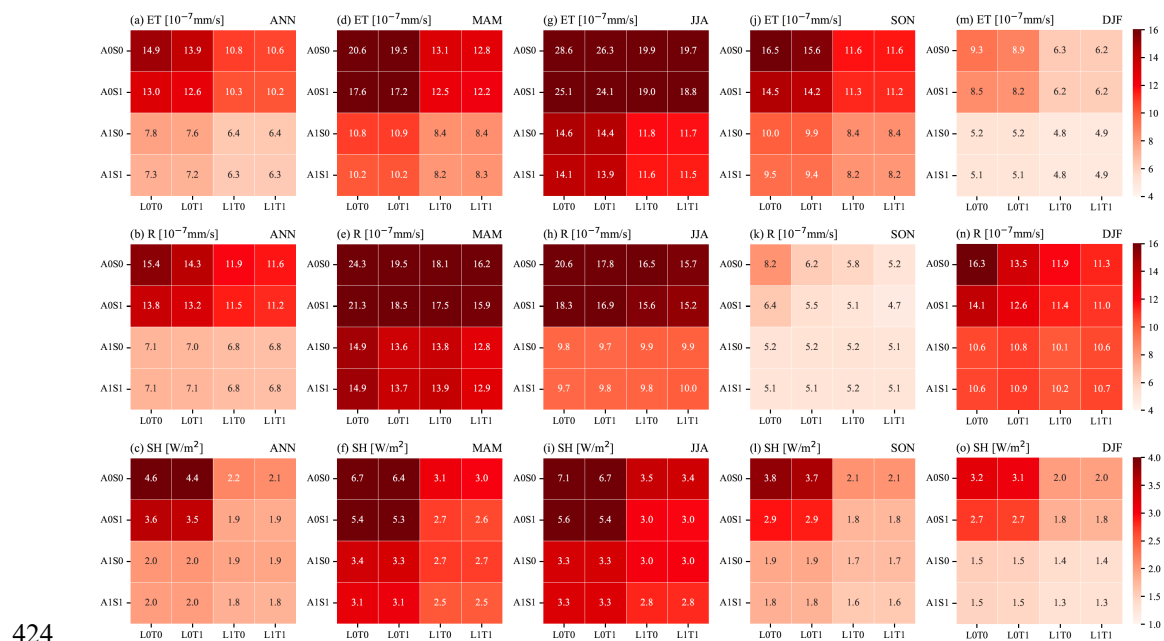
424

425   Figure 8. CONUS averaged absolute difference of SD between 16 ELM experiments and ERA5-

426   Land reanalysis for the annual (1st column) and seasonal (2nd – 5th column) climatological mean

427   of ET (top panel), R (middle panel), and SH (bottom panel).

428

429   **4. Discussions**

Geoscientific
Model Development
Discussions

430   ATM and LULC are the two most essential heterogeneity sources contributing to the spatial

431   variability of water and energy partitioning. Our results are consistent with Simon et al. (2020),

432   who found that the heterogeneous meteorological forcing is the primary driver for the spatial

433   variability of latent heat and sensible heat in WRF simulations. The Sobol' sensitivity index

434   averaged over the same region (a 100 km × 100 km domain centered at 36.6° N, 97.5° W) as Simon

435   et al. (2020) also indicates that ATM is the dominant heterogeneity source. Therefore, better

436   representation of ATM heterogeneity in climate models is crucial for modeling the water and

437   energy partitioning, especially for the three major components of precipitation, air temperature,

438   and longwave radiation. One approach of capturing ATM heterogeneity has been developed by

439   Tesfa et al. (2020) for downscaling the grid mean precipitation to topography-based subgrids for

440   land surface modeling. Besides ATM, LULC is the second most crucial heterogeneity source.

441   Notably, anthropogenic land use and land cover change has been shown to have large impacts on

442   land–atmosphere interaction, land surface hydrology, and associated extreme events (Findell et al.,

443   2017; Li et al., 2018, 2015; Swann et al., 2010; Zeng et al., 2017; Yuan et al., 2021; Pielke et al.,

444   2007). Therefore, the heterogeneity of LULC should also be well considered in climate modeling.

445

446   ATM and LULC show complementary contributions to the spatial variability of water and energy

447   partitioning spatially over CONUS and temporally in different seasons. Sobol' sensitivity analysis

448   is a standardized quantification of the relative importance of different heterogeneity sources. The

449   sum of the Sobol' indexes for the four heterogeneity sources roughly equals one. As the two

450   dominant heterogeneity sources, ATM Sobol index and LULC Sobol' index dominate the sum of

451   all Sobol' indexes. Hence, they show complementary patterns spatially (Figure 5) and temporally

452   (Figure 6). In addition, ATM and LULC show complementary contributions across different

453   climate zones. The Budyko's aridity index (BAI, Budyko 1974), which is the ratio of annual net

454   radiation to the product of the latent heat of water vaporization and the annual precipitation, was

455   calculated using the outputs from EXP16. From humid (low BAI) to arid climate (high BAI), a

456   decreasing fraction of the CONUS region is dominated by ATM in determining the ET/P spatial

457   variability (Figure 9a). At the same time, LULC shows an increasing contribution to the ET/P

458   spatial variability with BAI. The spatial variability of energy partitioning exhibits even more

459   complementarity between the ATM and LULC contributions from arid regions to humid regions

460   (Figure 9c). In more arid regions limited by water, EF spatial variability is much more dominated

461   by heterogeneity of ATM, likely through the heterogeneous precipitation, but in humid regions

462   limited by energy, LULC dominates the EF spatial variability through its influence on surface

463   albedo and surface roughness.
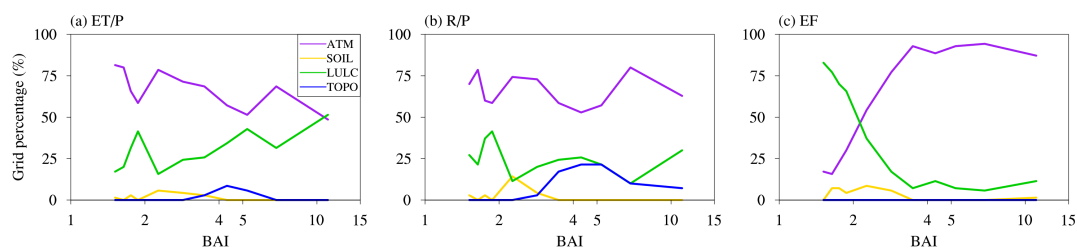
464

465   Figure 9. The grid percentage of dominant heterogeneity sources along with Budyko's aridity

466   index. A higher aridity index means more arid.

467

468   SOIL and TOPO show relatively small impacts on the spatial variability of water and energy

469   partitioning. However, TOPO has a dominant influence on the R/P spatial variability over the

470   transitional zone (Figure 9b) of central CONUS located between the arid western CONUS and the

471   humid eastern CONUS (Figure 4). SOIL shows some dominant effects on the spatial variability of

472   water and energy partitioning over a small proportion of humid regions (orange curve in Figure 9).

473   The heterogeneity in SOIL and TOPO was derived from coarse resolution data at 0.125°×0.125°

474   spatial resolution, which could be a possible reason for the minor SOIL and TOPO effects. Singh

475   et al. (2015) found that CLM4.0 did not show much improvement when model resolution increased

476   from ~100 km to ~25 km but improvement was noticeable at finer 1 km resolution. Additionally,

477   exclusion of lateral subsurface flow in ELMv1 could also lead to underestimation of the

478   contributions from SOIL and TOPO.

479

480   The current study excluded a few land surface processes that have been included in LSMs in the

481   last decade, limiting our ability to assess the role of land surface heterogeneity in spatiotemporal

482   variability of energy and water partitioning. For example, the hillslope processes of lateral ridge-

483   valley flow and the insolation contrasts between sunny and shady slopes are crucial for land surface

484   modeling (Fan et al., 2019; Taylor et al., 2012; Clark et al., 2015; Scheidegger et al., 2021), but

485   they are neglected in this study. Sean et al. (2019) incorporated the representative hillslope concept

486   into the CLM5, and they found that subgrid hillslope process induced large differences in

487   evapotranspiration between upland and lowland hillslope columns in arid and semiarid regions.

488   Krakauer et al. (2014) suggested that the magnitude of between-grid groundwater flow becomes

489   significant over larger regions at higher model resolution. Xie et al. (2020) also demonstrated the

490   importance of groundwater lateral flow in offsetting depression cones caused by intensive

491   groundwater pumping. Fang et al. (2017) compared the ACME Land Model (the earlier version of

492   ELM) and the three-dimensional ParFlow variably saturated flow model (Maxwell et al., 2015),

493   underscoring ELM limitation in capturing topography's influence on groundwater and runoff.

494   Additionally, topography also significantly influences insolation, including the shadow effects and

495   multi-scattering between adjacent terrain. Hao et al. (2021) implemented a sub-grid topographic

496   parameterization in ELM, which improves the simulated surface energy balance, snow cover, and

497   surface air temperature over the Tibetan Plateau. The inclusion of plant hydraulics has also shown

498   essential improvements in water and carbon simulations under drought conditions (Li et al., 2021;

499   Fang et al., 2021), which should also be considered in future research, especially as vegetation

500   may experience more hydroclimate drought stress in projected future climate conditions (Yuan et

501   al., 2019; Xu et al., 2019; Li et al., 2020). The subgrid downscaling of atmospheric forcing (Tesfa

502   et al., 2020), which could further enhance the representation of heterogeneity effects on water and

503   energy simulations, is also unaccounted for in this study.

504

505   **5. Conclusions**

506   This study comprehensively investigated the impacts of different heterogeneity sources (i.e., ATM,

507   LULC, SOIL, TOPO) on the spatial variability of water and energy partitioning over CONUS.

508   Two sets of experiments were conducted based on different combinations of spatially

509   heterogeneous and homogeneous datasets. Based on the first set of 16 experiments, Sobol' total

510   sensitivity analysis were utilized to identify the relative importance of the four heterogeneity

511   sources. The second set of 13 experiments were further used to assess the influence from individual

512   components of ATM, SOIL, and TOPO. Our results show that ATM and LULC are the two

513   dominant heterogeneity sources in determining the spatial variability of water and energy

514   partitioning. Their heterogeneity effects are spatially complementary across CONUS, and

515   temporally complementary across seasons. The complementary contributions of ATM and LULC

516   reflect the overall negligible impacts of SOIL and TOPO, but the complementarity also reflects

517   physically the clear demarcation of climatic zones across CONUS, featuring the arid, water-limited

518   western CONUS dominantly influenced by ATM (precipitation in particular) and the humid,

519   energy-limited eastern CONUS dominantly influenced by LULC. In the transitional climate zone

520   of central CONUS, TOPO shows some dominant influence on the R/P spatial variability. The

521   overall most essential components for ATM (precipitation, temperature, and longwave radiation),

522   SOIL (soil texture and soil color), and TOPO (Fmax) were also identified. Comparison with

523   ERA5-Land reanalysis reveals that accounting for more sources of heterogeneity improved the

524   simulated spatial variability of water and energy fluxes, although such improvements tend to

525   saturate as more heterogeneous sources were added.

526   The relative importance of different heterogeneity sources quantified in this study is useful for

527   prioritizing spatial heterogeneity to be included for improving land surface modeling. We note,

528   however, that the present assessment is limited by how well the input datasets capture the

529   spatiotemporal heterogeneity and how well the land surface model represent processes such as

530   hillslope hydrology and topographic effect on solar radiation that are influenced by land surface

531   heterogeneity. This motivates the use of more process-rich models such as distributed or three-

532   dimensional subsurface hydrology models to provide benchmarks of the relative importance of

533   heterogeneity sources to help prioritize future development of land surface models to improve

534   modeling of energy and water fluxes.

535

536   *Code and data availability*. The source code of ELMv1 is available from

537   https://github.com/E3SM-Project/E3SM (last access: September 2020); NLDAS-2 forcing is

538   available from https://ldas.gsfc.nasa.gov/nldas/v2/forcing; SOIL and TOPO related datasets are

539   downloaded from https://svn-ccsm-inputdata.cgd.ucar.edu/trunk/inputdata/lnd/clm2/rawdata/;

540   LULC related datasets are from Ke et al. (2012); ERA5-Land reanalysis is available from:

541   https://cds.climate.copernicus.eu/cdsapp#!/dataset/reanalysis-era5-land-monthly-

542   means?tab=overview.

543

544   *Author contributions*. LCL designed and conducted the experiments, analyzed model outputs, and

545   drafted the manuscript. GB designed the study, interpreted the results, and improved the

546   manuscript. LRL contributed to the interpretation and discussion of results and improvement of

547   the manuscript.

548

557

558   *Competing interests*. The authors declare that they have no conflict of interest.

Reference

Avissar, R. and Pielke, R. A.: A Parameterization of Heterogeneous Land Surfaces for Atmospheric Numerical Models and Its Impact on Regional Meteorology, Mon Weather Rev, 117, 2113–2136, https://doi.org/10.1175/1520-0493(1989)117<2113:apohls>2.0.co;2, 1989.

Baatz, R., Franssen, H. J. H., Euskirchen, E., Sihi, D., Dietze, M., Ciavatta, S., Fennel, K., Beck, H., Lannoy, G. D., Pauwels, V. R. N., Raiho, A., Montzka, C., Williams, M., Mishra, U., Poppe, C., Zacharias, S., Lausch, A., Samaniego, L., Looy, K. V., Bogena, H., Adamescu, M., Mirtl, M., Fox, A., Goergen, K., Naz, B. S., Zeng, Y., and Vereecken, H.: Reanalysis in Earth System Science: Toward Terrestrial Ecosystem Reanalysis, Rev Geophys, 59, https://doi.org/10.1029/2020rg000715, 2021.

Batjes, N. H.: Harmonized soil profile data for applications at global and continental scales: updates to the WISE database, Soil Use Manage, 25, 124–127, https://doi.org/10.1111/j.1475-2743.2009.00202.x, 2009.

Bierkens, M. F. P., Bell, V. A., Burek, P., Chaney, N., Condon, L. E., David, C. H., Roo, A. de, Döll, P., Drost, N., Famiglietti, J. S., Flörke, M., Gochis, D. J., Houser, P., Hut, R., Keune, J., Kollet, S., Maxwell, R. M., Reager, J. T., Samaniego, L., Sudicky, E., Sutanudjaja, E. H., Giesen, N. van de, Winsemius, H., and Wood, E. F.: Hyper-resolution global hydrological modelling: what is next?, 29, 310–320, https://doi.org/10.1002/hyp.10391, 2014.

Bisht, G., Riley, W. J., Hammond, G. E., and Lorenzetti, D. M.: Development and evaluation of a variably saturated flow model in the global E3SM Land Model (ELM) version 1.0, Geosci Model Dev, 11, 4085–4102, https://doi.org/10.5194/gmd-11-4085-2018, 2018.

Bonan, G. B., Levis, S., Kergoat, L., and Oleson, K. W.: Landscapes as patches of plant functional types: An integrating concept for climate and ecosystem models, Global Biogeochem Cy, 16, 5-1-5–23, https://doi.org/10.1029/2000gb001360, 2002.

Budyko, M. I. (1974). Climate and life, (p. 508). New York: Academic Press.

Caldwell, P. M., Mametjanov, A., Tang, Q., Roekel, L. P. V., Golaz, J., Lin, W., Bader, D. C., Keen, N. D., Feng, Y., Jacob, R., Maltrud, M. E., Roberts, A. F., Taylor, M. A., Veneziani, M., Wang, H., Wolfe, J. D., Balaguru, K., Cameron-Smith, P., Dong, L., Klein, S. A., Leung, L. R., Li, H., Li, Q., Liu, X., Neale, R. B., Pinheiro, M., Qian, Y., Ullrich, P. A., Xie, S., Yang, Y., Zhang, Y., Zhang, K., and Zhou, T.: The DOE E3SM Coupled Model Version 1: Description and Results at High Resolution, J Adv Model Earth Sy, 11, 4095–4146, https://doi.org/10.1029/2019ms001870, 2019.

Chaney, N. W., Metcalfe, P., and Wood, E. F.: HydroBlocks: a field-scale resolving land surface model for application over continental extents, Hydrol Process, 30, 3543–3559, https://doi.org/10.1002/hyp.10891, 2016.

Chaney, N. W., Huijgevoort, M. H. J. V., Shevliakova, E., Malyshev, S., Milly, P. C. D., Gauthier, P. P. G., and Sulman, B. N.: Harnessing big data to rethink land heterogeneity in Earth system models, Hydrol Earth Syst Sc, 22, 3311–3330, https://doi.org/10.5194/hess-22-3311-2018, 2018.

Clark, M. P., Fan, Y., Lawrence, D. M., Adam, J. C., Bolster, D., Gochis, D. J., Hooper, R. P., Kumar, M., Leung, L. R., Mackay, D. S., Maxwell, R. M., Shen, C., Swenson, S. C., and Zeng, X.: Improving the representation of hydrologic processes in Earth System Models, 51, 5929–5956, https://doi.org/10.1002/2015wr017096, 2015.

603   Cuesta-Valero, F. J., García-García, A., Beltrami, H., González-Rouco, F., and García-
604   Bustamante, E.: WRF v.3.9 sensitivity to land surface model and horizontal resolution
605   changes over North America, Geosci Model Dev, https://doi.org/10.5194/gmd-2021-243,
606   2020.

607   Dai, H., Ye, M., Walker, A. P., and Chen, X.: A new process sensitivity index to identify
608   important system processes under process model and parametric uncertainty, Water Resour
609   Res, 53, 3476–3490, https://doi.org/10.1002/2016wr019715, 2017.

610   Essery, R. L. H., Best, M. J., Betts, R. A., Cox, P. M., and Taylor, C. M.: Explicit Representation
611   of Subgrid Heterogeneity in a GCM Land Surface Scheme, J Hydrometeorol, 4, 530–543,
612   https://doi.org/10.1175/1525-7541(2003)004<0530:eroshi>2.0.co;2, 2003.

613   Fan, Y., Clark, M., Lawrence, D. M., Swenson, S., Band, L. E., Brantley, S. L., Brooks, P. D.,
614   Dietrich, W. E., Flores, A., Grant, G., Kirchner, J. W., Mackay, D. S., McDonnell, J. J.,
615   Milly, P. C. D., Sullivan, P. L., Tague, C., Ajami, H., Chaney, N., Hartmann, A.,
616   Hazenberg, P., McNamara, J., Pelletier, J., Perket, J., Rouholahnejad-Freund, E., Wagener,
617   T., Zeng, X., Beighley, E., Buzan, J., Huang, M., Livneh, B., Mohanty, B. P., Nijssen, B.,
618   Safeeq, M., Shen, C., Verseveld, W., Volk, J., and Yamazaki, D.: Hillslope Hydrology in
619   Global Change Research and Earth System Modeling, Water Resour Res, 55, 1737–1772,
620   https://doi.org/10.1029/2018wr023903, 2019.

621   Fang, Y., Leung, L. R., Duan, Z., Wigmosta, M. S., Maxwell, R. M., Chambers, J. Q., and
622   Tomasella, J.: Influence of landscape heterogeneity on water available to tropical forests in
623   an Amazonian catchment and implications for modeling drought response, 122, 8410–8426,
624   https://doi.org/10.1002/2017jd027066, 2017.

625   Fang, Y., Leung, L. R., Wolfe, B. T., Detto, M., Knox, R. G., McDowell, N. G., Grossiord, C.,
626   Xu, C., Christoffersen, B. O., Gentine, P., Koven, C. D., and Chambers, J. Q.: Disentangling
627   the Effects of Vapor Pressure Deficit and Soil Water Availability on Canopy Conductance
628   in a Seasonal Tropical Forest During the 2015 El Niño Drought, J Geophys Res
629   Atmospheres, 126, https://doi.org/10.1029/2021jd035004, 2021.

630   Findell, K. L., Berg, A., Gentine, P., Krasting, J. P., Lintner, B. R., Malyshev, S., Santanello, J.
631   A., and Shevliakova, E.: The impact of anthropogenic land use and land cover change on
632   regional climate extremes, 8, 989, https://doi.org/10.1038/s41467-017-01038-w, 2017.

633   Fisher, R. A. and Koven, C. D.: Perspectives on the Future of Land Surface Models and the
634   Challenges of Representing Complex Terrestrial Systems, J Adv Model Earth Sy, 12,
635   https://doi.org/10.1029/2018ms001453, 2020.

636   Garnaud, C., Bélair, S., Berg, A., and Rowlandson, T.: Hyperresolution Land Surface Modeling
637   in the Context of SMAP Cal–Val, J Hydrometeorol, 17, 345–352,
638   https://doi.org/10.1175/jhm-d-15-0070.1, 2016.

639   Giorgi, F. and Avissar, R.: Representation of heterogeneity effects in Earth system modeling:
640   Experience from land surface modeling, Rev Geophys, 35, 413–437,
641   https://doi.org/10.1029/97rg01754, 1997.

642   Golaz, J., Caldwell, P. M., Roekel, L. P. V., Petersen, M. R., Tang, Q., Wolfe, J. D., Abeshu, G.,
643   Anantharaj, V., Asay-Davis, X. S., Bader, D. C., Baldwin, S. A., Bisht, G., Bogenschutz, P.
644   A., Branstetter, M., Brunke, M. A., Brus, S. R., Burrows, S. M., Cameron-Smith, P. J.,
645   Donahue, A. S., Deakin, M., Easter, R. C., Evans, K. J., Feng, Y., Flanner, M., Foucar, J. G.,
646   Fyke, J. G., Griffin, B. M., Hannay, C., Harrop, B. E., Hoffman, M. J., Hunke, E. C., Jacob,

647   R. L., Jacobsen, D. W., Jeffery, N., Jones, P. W., Keen, N. D., Klein, S. A., Larson, V. E.,
648   Leung, L. R., Li, H., Lin, W., Lipscomb, W. H., Ma, P., Mahajan, S., Maltrud, M. E.,
649   Mametjanov, A., McClean, J. L., McCoy, R. B., Neale, R. B., Price, S. F., Qian, Y., Rasch,
650   P. J., Eyre, J. E. J. R., Riley, W. J., Ringler, T. D., Roberts, A. F., Roesler, E. L., Salinger,
651   A. G., Shaheen, Z., Shi, X., Singh, B., Tang, J., Taylor, M. A., Thornton, P. E., Turner, A.
652   K., Veneziani, M., Wan, H., Wang, H., Wang, S., Williams, D. N., Wolfram, P. J., Worley,
653   P. H., Xie, S., Yang, Y., Yoon, J., Zelinka, M. D., Zender, C. S., Zeng, X., Zhang, C.,
654   Zhang, K., Zhang, Y., Zheng, X., Zhou, T., and Zhu, Q.: The DOE E3SM Coupled Model
655   Version 1: Overview and Evaluation at Standard Resolution, J Adv Model Earth Sy, 11,
656   2089–2129, https://doi.org/10.1029/2018ms001603, 2019.

657   Hao, D., Bisht, G., Gu, Y., Lee, W., Liou, K.-N., and Leung, L. R.: A Parameterization of Sub-
658   grid Topographical Effects on Solar Radiation in the E3SM Land Model (Version 1.0):
659   Implementation and Evaluation Over the Tibetan Plateau, Geoscientific Model Dev Discuss,
660   2021, 1–23, https://doi.org/10.5194/gmd-2021-55, 2021.

661   He, S., Smirnova, T. G., and Benjamin, S. G.: Single-Column Validation of a Snow Subgrid
662   Parameterization in the Rapid Update Cycle Land-Surface Model (RUC LSM), Water
663   Resour Res, 57, https://doi.org/10.1029/2021wr029955, 2021.

664   Homma, T. and Saltelli, A.: Importance measures in global sensitivity analysis of nonlinear
665   models, Reliab Eng Syst Safe, 52, 1–17, https://doi.org/10.1016/0951-8320(96)00002-6,
666   1996.

667   Hugelius, G., Tarnocai, C., Broll, G., Canadell, J. G., Kuhry, P., and Swanson, D. K.: The
668   Northern Circumpolar Soil Carbon Database: spatially distributed datasets of soil coverage
669   and soil carbon storage in the northern permafrost regions, Earth Syst Sci Data, 5, 3–13,
670   https://doi.org/10.5194/essd-5-3-2013, 2013.

671   Ji, P., Yuan, X., and Liang, X.: Do Lateral Flows Matter for the Hyperresolution Land Surface
672   Modeling?, J Geophys Res Atmospheres, 122, 12,077-12,092,
673   https://doi.org/10.1002/2017jd027366, 2017.

674   Jr., J. A. S., Dirmeyer, P. A., Ferguson, C. R., Findell, K. L., Tawfik, A. B., Berg, A., Ek, M.,
675   Gentine, P., Guillod, B. P., Heerwaarden, C. van, Roundy, J., and Wulfmeyer, V.: Land-
676   Atmosphere Interactions: The LoCo Perspective, B Am Meteorol Soc, 99, 1253–1272,
677   https://doi.org/10.1175/bams-d-17-0001.1, 2017.

678   Ke, Y., Leung, L. R., Huang, M., Coleman, A. M., Li, H., and Wigmosta, M. S.: Development of
679   high resolution land surface parameters for the Community Land Model, Geosci Model
680   Dev, 5, 1341–1362, https://doi.org/10.5194/gmd-5-1341-2012, 2012.

681   Klingler, C., Schulz, K., and Herrnegger, M.: LamaH-CE: LArge-SaMple DAta for Hydrology
682   and Environmental Sciences for Central Europe, Earth Syst Sci Data, 13, 4529–4565,
683   https://doi.org/10.5194/essd-13-4529-2021, 2021.

684   Ko, A., Mascaro, G., and Vivoni, E. R.: Strategies to Improve and Evaluate Physics-Based
685   Hyperresolution Hydrologic Simulations at Regional Basin Scales, Water Resour Res, 55,
686   1129–1152, https://doi.org/10.1029/2018wr023521, 2019.

687   Koster, R. D., Hahmann, A. N., Ijpelaar, R., Tyahla, L., Suarez, M. J., Dirmeyer, P. A.,
688   Hahmann, A. N., Ijpelaar, R., Tyahla, L., Cox, P., and Suarez, M. J.: Comparing the Degree
689   of Land–Atmosphere Interaction in Four Atmospheric General Circulation Models, 3, 363–
690   375, https://doi.org/10.1175/1525-7541(2002)003<0363:ctdola>2.0.co;2, 2002.

691   Krakauer, N. Y., Li, H., and Fan, Y.: Groundwater flow across spatial scales: importance for
692   climate modeling, Environ Res Lett, 9, 034003, https://doi.org/10.1088/1748-
693   9326/9/3/034003, 2014.

694   Lawrence, D. M. and Slater, A. G.: Incorporating organic soil into a global climate model, Clim
695   Dynam, 30, 145–160, https://doi.org/10.1007/s00382-007-0278-1, 2008.

696   Lawrence, D. M., Fisher, R. A., Koven, C. D., Oleson, K. W., Swenson, S. C., Bonan, G.,
697   Collier, N., Ghimire, B., Kampenhout, L., Kennedy, D., Kluzek, E., Lawrence, P. J., Li, F.,
698   Li, H., Lombardozzi, D., Riley, W. J., Sacks, W. J., Shi, M., Vertenstein, M., Wieder, W. R.,
699   Xu, C., Ali, A. A., Badger, A. M., Bisht, G., Broeke, M., Brunke, M. A., Burns, S. P.,
700   Buzan, J., Clark, M., Craig, A., Dahlin, K., Drewniak, B., Fisher, J. B., Flanner, M., Fox, A.
701   M., Gentine, P., Hoffman, F., Keppel-Aleks, G., Knox, R., Kumar, S., Lenaerts, J., Leung,
702   L. R., Lipscomb, W. H., Lu, Y., Pandey, A., Pelletier, J. D., Perket, J., Randerson, J. T.,
703   Ricciuto, D. M., Sanderson, B. M., Slater, A., Subin, Z. M., Tang, J., Thomas, R. Q.,
704   Martin, M. V., and Zeng, X.: The Community Land Model Version 5: Description of New
705   Features, Benchmarking, and Impact of Forcing Uncertainty, J Adv Model Earth Sy, 11,
706   4245–4287, https://doi.org/10.1029/2018ms001583, 2019.

707   Lawrence, P. J. and Chase, T. N.: Representing a new MODIS consistent land surface in the
708   Community Land Model (CLM 3.0), J Geophys Res Biogeosciences 2005 2012, 112,
709   https://doi.org/10.1029/2006jg000168, 2007.

710   Leung, L. R., Bader, D. C., Taylor, M. A., and McCoy, R. B.: An Introduction to the E3SM
711   Special Collection: Goals, Science Drivers, Development, and Analysis, J Adv Model Earth
712   Sy, 12, https://doi.org/10.1029/2019ms001821, 2020.

713   Li, H., Wigmosta, M. S., Wu, H., Huang, M., Ke, Y., Coleman, A. M., and Leung, L. R.: A
714   Physically Based Runoff Routing Model for Land Surface and Earth System Models, J
715   Hydrometeorol, 14, 808–828, https://doi.org/10.1175/jhm-d-12-015.1, 2013a.

716   Li, J., Duan, Q. Y., Gong, W., Ye, A., Dai, Y., Miao, C., Di, Z., Tong, C., and Sun, Y.:
717   Assessing parameter importance of the Common Land Model based on qualitative and
718   quantitative sensitivity analysis, Hydrol Earth Syst Sc, 17, 3279–3293,
719   https://doi.org/10.5194/hess-17-3279-2013, 2013b.

720   Li, L., Zhang, L., Xia, J., Gippel, C. J., Wang, R., and Zeng, S.: Implications of Modelled
721   Climate and Land Cover Changes on Runoff in the Middle Route of the South to North
722   Water Transfer Project in China, 29, 2563–2579, https://doi.org/10.1007/s11269-015-0957-
723   3, 2015.

724   Li, L., She, D., Zheng, H., Lin, P., and Yang, Z. L.: Elucidating Diverse Drought Characteristics
725   from Two Meteorological Drought Indices (SPI and SPEI) in China, 21, 1513–1530,
726   https://doi.org/10.1175/jhm-d-19-0290.1, 2020.

727   Li, L., Yang, Z., Matheny, A. M., Zheng, H., Swenson, S. C., Lawrence, D. M., Barlage, M.,
728   Yan, B., McDowell, N. G., and Leung, L. R.: Representation of Plant Hydraulics in the
729   Noah-MP Land Surface Model: Model Development and Multiscale Evaluation, J Adv
730   Model Earth Sy, 13, https://doi.org/10.1029/2020ms002214, 2021.

731   Li, Y., Piao, S., Li, L. Z. X., Chen, A., and Zhou, L.: Divergent hydrological response to large-
732   scale afforestation and vegetation greening in China, 4, eaar4182,
733   https://doi.org/10.1126/sciadv.aar4182, 2018.

734 Lindstedt, D., Lind, P., Kjellström, E., and Jones, C.: A new regional climate model operating at
735   the meso-gamma scale: performance over Europe, Tellus, 67, 24138,
736   https://doi.org/10.3402/tellusa.v67.24138, 2015.
737 Liu, S., Shao, Y., Kunoth, A., and Simmer, C.: Impact of surface-heterogeneity on atmosphere
738   and land-surface interactions, Environ Modell Softw, 88, 35–47,
739   https://doi.org/10.1016/j.envsoft.2016.11.006, 2017.
740 Maxwell, R. M., Condon, L. E., and Kollet, S. J.: A high-resolution simulation of groundwater
741   and surface water over most of the continental US with the integrated hydrologic model
742   ParFlow v3, Geosci Model Dev, 8, 923–937, https://doi.org/10.5194/gmd-8-923-2015,
743   2015.
744 Muñoz-Sabater, J., Dutra, E., Agustí-Panareda, A., Albergel, C., Arduini, G., Balsamo, G.,
745   Boussetta, S., Choulga, M., Harrigan, S., Hersbach, H., Martens, B., Miralles, D. G., Piles,
746   M., Rodríguez-Fernández, N. J., Zsoter, E., Buontempo, C., and Thépaut, J.-N.: ERA5-
747   Land: a state-of-the-art global reanalysis dataset for land applications, Earth Syst Sci Data,
748   13, 4349–4383, https://doi.org/10.5194/essd-13-4349-2021, 2021.
749 Naz, B. S., Kurtz, W., Montzka, C., Sharples, W., Goergen, K., Keune, J., Gao, H., Springer, A.,
750   Franssen, H.-J. H., and Kollet, S.: Improving soil moisture and runoff simulations at 3 km
751   over Europe using land surface data assimilation, Hydrol Earth Syst Sc, 23, 277–301,
752   https://doi.org/10.5194/hess-23-277-2019, 2018.
753 Niu, G., Yang, Z., Dickinson, R. E., and Gulden, L. E.: A simple TOPMODEL-based runoff
754   parameterization (SIMTOP) for use in global climate models, J Geophys Res Atmospheres
755   1984 2012, 110, https://doi.org/10.1029/2005jd006111, 2005.
756 Nossent, J., Elsen, P., and Bauwens, W.: Sobol' sensitivity analysis of a complex environmental
757   model, Environ Modell Softw, 26, 1515–1525,
758   https://doi.org/10.1016/j.envsoft.2011.08.010, 2011.
759 Oleson, K. W., Lawrence, D. M., Bonan, G. B., Drewniak, B., Huang, M., Koven, C. D., Levis,
760   S., Li, F., Riley, W. J., Subin, Z. M., Swenson, S. C., Thornton, P. E., Bozbiyik, A., Fisher,
761   R., Heald, C. L., Kluzek, E., Lamarque, J.-F., Lawrence, P. J., Leung, L. R., Lipscomb, W.,
762   Muszala, S., Ricciuto, D. M., Sacks, W., Sun, Y., Tang, J., Yang, Z.-L. (2013). Technical
763   description of version 4.5 of the Community Land Model (CLM) (NCAR Technical Note
764   NCAR/TN-503 + STR). Retrieved from Boulder, Colorado:
765   https://doi.org/10.5065/D6RR1W7M
766 PIELKE, R. A., ADEGOKE, J., BELTRÁN-PRZEKURAT, A., HIEMSTRA, C. A., LIN, J.,
767   NAIR, U. S., NIYOGI, D., and NOBIS, T. E.: An overview of regional land-use and land-
768   cover impacts on rainfall, Tellus B, 59, 587–601, https://doi.org/10.1111/j.1600-
769   0889.2007.00251.x, 2007.
770 Rosolem, R., Gupta, H. V., Shuttleworth, W. J., Zeng, X., and Gonçalves, L. G. G.: A fully
771   multiple-criteria implementation of the Sobol′ method for parameter sensitivity analysis, J
772   Geophys Res Atmospheres 1984 2012, 117, n/a-n/a, https://doi.org/10.1029/2011jd016355,
773   2012.
774 Rouf, T., Maggioni, V., Mei, Y., and Houser, P.: Towards hyper-resolution land-surface
775   modeling of surface and root zone soil moisture, J Hydrol, 594, 125945,
776   https://doi.org/10.1016/j.jhydrol.2020.125945, 2021.

Rummukainen, M.: Added value in regional climate modeling, Wiley Interdiscip Rev Clim Change, 7, 145–159, https://doi.org/10.1002/wcc.378, 2016.

Saltelli, A.: Sensitivity Analysis for Importance Assessment, Risk Anal, 22, 579–590, https://doi.org/10.1111/0272-4332.00040, 2002.

Saltelli, A. and Tarantola, S.: On the Relative Importance of Input Factors in Mathematical Models, J Am Stat Assoc, 97, 702–709, https://doi.org/10.1198/016214502388618447, 2011.

Saltelli, A., Aleksankina, K., Becker, W., Fennell, P., Ferretti, F., Holst, N., Li, S., and Wu, Q.: Why so many published sensitivity analyses are false: A systematic review of sensitivity analysis practices, Environ Modell Softw, 114, 29–39, https://doi.org/10.1016/j.envsoft.2019.01.012, 2019.

Scheidegger, J. M., Jackson, C. R., Muddu, S., Tomer, S. K., and Filgueira, R.: Integration of 2D Lateral Groundwater Flow into the Variable Infiltration Capacity (VIC) Model and Effects on Simulated Fluxes for Different Grid Resolutions and Aquifer Diffusivities, Water-sui, 13, 663, https://doi.org/10.3390/w13050663, 2021.

Senf, C. and Seidl, R.: Persistent impacts of the 2018 drought on forest disturbance regimes in Europe, Biogeosciences Discuss, 2021, 1–10, https://doi.org/10.5194/bg-2021-120, 2021.

Simon, J. S., Bragg, A. D., Dirmeyer, P. A., and Chaney, N. W.: Semi-coupling of a Field-scale Resolving Land-surface Model and WRF-LES to Investigate the Influence of Land-surface Heterogeneity on Cloud Development, https://doi.org/10.1002/essoar.10507168.1, 2020.

Singh, R. S., Reager, J. T., Miller, N. L., and Famiglietti, J. S.: Toward hyper-resolution land-surface modeling: The effects of fine-scale topography and soil texture on CLM4.0 simulations over the Southwestern U.S., Water Resour Res, 51, 2648–2667, https://doi.org/10.1002/2014wr015686, 2015.

Swann, A. L., Fung, I. Y., Levis, S., Bonan, G. B., and Doney, S. C.: Changes in Arctic vegetation amplify high-latitude warming through the greenhouse effect., 107, 1295–1300, https://doi.org/10.1073/pnas.0913846107, 2010.

Swenson, S. C., Clark, M., Fan, Y., Lawrence, D. M., and Perket, J.: Representing Intrahillslope Lateral Subsurface Flow in the Community Land Model, J Adv Model Earth Sy, 11, 4044–4065, https://doi.org/10.1029/2019ms001833, 2019.

Sobol', I. M. (1993). Sensitivity analysis for nonlinear mathematical models [English translation]. Mathematical Modelling and Computational Experiment, 1, 407–414.

Taylor, R. G., Scanlon, B., Döll, P., Rodell, M., Beek, R. van, Wada, Y., Longuevergne, L., Leblanc, M., Famiglietti, J. S., Edmunds, M., Konikow, L., Green, T. R., Chen, J., Taniguchi, M., Bierkens, M. F., MacDonald, A., Fan, Y., Maxwell, R. M., Yechieli, Y., Gurdak, J. J., Allen, D. M., Shamsudduha, M., Hiscock, K., Yeh, P., Holman, I., and Treidel, H.: Ground water and climate change, 3, 322–329, https://doi.org/10.1038/nclimate1744, 2012.

Tesfa, T. K. and Leung, L.-Y. R.: Exploring new topography-based subgrid spatial structures for improving land surface modeling, Geosci Model Dev, 10, 873–888, https://doi.org/10.5194/gmd-10-873-2017, 2017.

Tesfa, T. K., Li, H.-Y., Leung, L. R., Huang, M., Ke, Y., Sun, Y., and Liu, Y.: A subbasin-based framework to represent land surface processes in an Earth system model, Geosci Model Dev, 7, 947–963, https://doi.org/10.5194/gmd-7-947-2014, 2014a.

821 Tesfa, T. K., Leung, L. R., Huang, M., Li, H., Voisin, N., and Wigmosta, M. S.: Scalability of
822   grid- and subbasin-based land surface modeling approaches for hydrologic simulations, J
823   Geophys Res Atmospheres, 119, 3166–3184, https://doi.org/10.1002/2013jd020493, 2014.
824 Tesfa, T. K., Leung, L. R., and Ghan, S. J.: Exploring Topography-Based Methods for
825   Downscaling Subgrid Precipitation for Use in Earth System Models, J Geophys Res
826   Atmospheres, 125, https://doi.org/10.1029/2019jd031456, 2020.
827 Torma, C., Giorgi, F., and Coppola, E.: Added value of regional climate modeling over areas
828   characterized by complex terrain—Precipitation over the Alps, J Geophys Res Atmospheres,
829   120, 3957–3972, https://doi.org/10.1002/2014jd022781, 2015.
830 Tramblay, Y., Villarini, G., Khalki, E. M., Gründemann, G., and Hughes, D.: Evaluation of the
831   Drivers Responsible for Flooding in Africa, Water Resour Res, 57,
832   https://doi.org/10.1029/2021wr029595, 2021.
833 Vegas-Cañas, C., González-Rouco, J. F., Navarro-Montesinos, J., García-Bustamante, E., Lucio-
834   Eceiza, E. E., García-Pereira, F., Rodríguez-Camino, E., Chazarra-Bernabé, A., and
835   Álvarez-Arévalo, I.: An Assessment of Observed and Simulated Temperature Variability in
836   Sierra de Guadarrama, Atmosphere-basel, 11, 985, https://doi.org/10.3390/atmos11090985,
837   2020.
838 Vergopolan, N., Chaney, N. W., Beck, H. E., Pan, M., Sheffield, J., Chan, S., and Wood, E. F.:
839   Combining hyper-resolution land surface modeling with SMAP brightness temperatures to
840   obtain 30-m soil moisture estimates, Remote Sens Environ, 242, 111740,
841   https://doi.org/10.1016/j.rse.2020.111740, 2020.
842 Verdin, K. L., and S. K. Greenlee, 1996. Development of continental scale digital elevation
843   models and extraction of hydrographic features, paper presented at the Third International
844   Conference/Workshop on Integrating GIS and Environmental Modeling, Santa Fe, New
845   Mexico, 21–26 January, Natl. Cent. for Geogr. Inf. and Anal., Santa Barbara, Calif.
846 Xia, Y., Mitchell, K., Ek, M., Cosgrove, B., Sheffield, J., Luo, L., Alonge, C., Wei, H., Meng, J.,
847   Livneh, B., Duan, Q., and Lohmann, D.: Continental-scale water and energy flux analysis
848   and validation for North American Land Data Assimilation System project phase 2
849   (NLDAS-2): 2. Validation of model-simulated streamflow, J Geophys Res Atmospheres
850   1984 2012, 117, https://doi.org/10.1029/2011jd016051, 2012a.
851 Xia, Y., Mitchell, K., Ek, M., Sheffield, J., Cosgrove, B., Wood, E., Luo, L., Alonge, C., Wei,
852   H., Meng, J., Livneh, B., Lettenmaier, D., Koren, V., Duan, Q., Mo, K., Fan, Y., and
853   Mocko, D.: Continental-scale water and energy flux analysis and validation for the North
854   American Land Data Assimilation System project phase 2 (NLDAS-2): 1. Intercomparison
855   and application of model products: WATER AND ENERGY FLUX ANALYSIS, J
856   Geophys Res Atmospheres, 117, n/a-n/a, https://doi.org/10.1029/2011jd016048, 2012b.
857 Xie, Z., Wang, L., Wang, Y., Liu, B., Li, R., Xie, J., Zeng, Y., Liu, S., Gao, J., Chen, S., Jia, B.,
858   and Qin, P.: Land Surface Model CAS-LSM: Model Description and Evaluation, J Adv
859   Model Earth Sy, 12, https://doi.org/10.1029/2020ms002339, 2020.
860 Xu, C., McDowell, N. G., Fisher, R. A., Wei, L., Sevanto, S., Christoffersen, B. O., Weng, E.,
861   and Middleton, R. S.: Increasing impacts of extreme droughts on vegetation productivity
862   under climate change, Nat Clim Change, 9, 948–953, https://doi.org/10.1038/s41558-019-
863   0630-6, 2019.

864 Xue, Y., Houser, P. R., Maggioni, V., Mei, Y., Kumar, S. V., and Yoon, Y.: Evaluation of High
865   Mountain Asia-Land Data Assimilation System (Version 1) From 2003 to 2016, Part I: A
866   Hyper-Resolution Terrestrial Modeling System, J Geophys Res Atmospheres, 126,
867   https://doi.org/10.1029/2020jd034131, 2021.
868 Yang, X., Ricciuto, D. M., Thornton, P. E., Shi, X., Xu, M., Hoffman, F., and Norby, R. J.: The
869   Effects of Phosphorus Cycle Dynamics on Carbon Sources and Sinks in the Amazon
870   Region: A Modeling Study Using ELMv1, J Geophys Res Biogeosciences, 124, 3686–3698,
871   https://doi.org/10.1029/2019jg005082, 2019.
872 Yuan, K., Zhu, Q., Zheng, S., Zhao, L., Chen, M., Riley, W. J., Cai, X., Ma, H., Li, F., Wu, H.,
873   and Chen, L.: Deforestation reshapes land-surface energy-flux partitioning, Environ Res
874   Lett, 16, 024014, https://doi.org/10.1088/1748-9326/abd8f9, 2021.
875 Yuan, W., Zheng, Y., Piao, S., Ciais, P., Lombardozzi, D., Wang, Y., Ryu, Y., Chen, G., Dong,
876   W., Hu, Z., Jain, A. K., Jiang, C., Kato, E., Li, S., Lienert, S., Liu, S., Nabel, J. E. M. S.,
877   Qin, Z., Quine, T., Sitch, S., Smith, W. K., Wang, F., Wu, C., Xiao, Z., and Yang, S.:
878   Increased atmospheric vapor pressure deficit reduces global vegetation growth, 5, eaax1396,
879   https://doi.org/10.1126/sciadv.aax1396, 2019.
880 Yuan, X., Ji, P., Wang, L., Liang, X., Yang, K., Ye, A., Su, Z., and Wen, J.: High-Resolution
881   Land Surface Modeling of Hydrological Changes Over the Sanjiangyuan Region in the
882   Eastern Tibetan Plateau: 1. Model Development and Evaluation, J Adv Model Earth Sy, 10,
883   2806–2828, https://doi.org/10.1029/2018ms001412, 2018.
884 Zeng, Z., Piao, S., Li, L., Zhou, L., CIAIS, P., and Wang, T.: Climate mitigation from vegetation
885   biophysical feedbacks during the past three decades, 2017.
886 Zheng, H., Yang, Z., Lin, P., Wei, J., Wu, W., Li, L., Zhao, L., and Wang, S.: On the Sensitivity
887   of the Precipitation Partitioning Into Evapotranspiration and Runoff in Land Surface
888   Parameterizations, Water Resour Res, 55, 95–111, https://doi.org/10.1029/2017wr022236,
889   2019.
890 Zhou, T., Leung, L. R., Leng, G., Voisin, N., Li, H., Craig, A. P., Tesfa, T., and Mao, Y.: Global
891   Irrigation Characteristics and Effects Simulated by Fully Coupled Land Surface, River, and
892   Water Management Models in E3SM, J Adv Model Earth Sy, 12,
893   https://doi.org/10.1029/2020ms002069, 2020.
894 Zhou, Y., Li, D., and Li, X.: The Effects of Surface Heterogeneity Scale on the Flux Imbalance
895   under Free Convection, J Geophys Res Atmospheres, 124, 8424–8448,
896   https://doi.org/10.1029/2018jd029550, 2019.